Surfaces and Interfaces 24 (2021) 101036

Contents lists available at ScienceDirect

Surfaces and Interfaces

journal homepage: www.sciencedirect.com/journal/surfaces-and-interfaces

Ab initio insights into Graphene-Zirconium disulfide/diselenide heterostructure as electrode material for alkali-ion batteries

Gladys W. King'ori [a,b,*], Cecil N M Ouma [c], George O. Amolo [b], Nicholas W. Makau [a]

[a] University of Eldoret, P.O Box. 1125–30100, Eldoret, Kenya
[b] Technical University of Kenya, Haile Selassie Avenue, P.O Box 52428–00200, Nairobi, Kenya
[c] HySA-Infrastructure, North-West University, Faculty of Engineering, Private Bag X6001, Potchefstroom, South Africa, 2520

A B S T R A C T

In the search for an energy storage medium with higher electronic conductivity, rate performance and moderate volume expansion, van der Waals heterostructures are a promising alternative. Herein, the potential of graphene (Gr) and Zirconium dichalcogenide (ZrX_2, X = S, Se) van der Waals heterostructures for applications as battery electrodes is explored using density functional theory (DFT) calculations. Through intercalating alkali ions (Li and K) between the Gr and ZrX_2, we obtain low energy activation barriers, indicating that Gr-ZrX_2 van der Waals heterostructures can be candidates for high rate performance electrode application.

DFT calculations also indicate that the Gr-ZrX_2 heterostructure formation is energetically favoured with better volume expansion as compared to bilayer Gr and ZrX_2. The calculated open circuit voltage (OCV) for K intercalation was 0.66 V (Gr-$ZrSe_2$) and 0.77 V (Gr-ZrS_2), hence suitable for anodic application in Potassium-ion batteries (KIB). The calculated OCV for Li interaction was 2.83 V (Gr-$ZrSe_2$) and 2.95 V (Gr-ZrS_2) hence suitable for cathodic applications.

1. Introduction

Efficient alkali ion batteries require high electronic and ionic conductivity, specific energy density and cycling stability [1,2]. However, current Lithium ion batteries (LIBs) are unable to meet this demand [1]. In response to this need, theoretical calculations based on first principles, such as, density functional theory (DFT) have been used to explore the potential of two-dimensional systems and van der Waals heterostructures as battery materials [3–6]. Two-dimensional layered materials (2DLMs) have courted attention since the discovery of graphene (Gr) due to their novel properties. Beyond Gr, there is a wide spectrum of 2D electronic materials that range from; semiconductors such as ZrS_2 [7], $ZrSe_2$ [8,9], HfS_2 [3,10], δ-phosphorene [11], blue phosphorene [12] and MoS_2 [13,14]; to semimetals WTe_2 [15], $TiSe_2$ [16], among others; to NbS_2 [17], VSe_2 [18], which are true metals; to insulators such as boron nitride [19] and also to superconductors including $NbSe_2$ [20], TaS_2 [21], depending on their composition.

This extensive collection of 2DLMs with selectable and/or tunable material properties opens up the prospect of heterogeneous combinations at the atomic scale and hence creating novel hybrid structures such as MoS_2/ZnO [22] that display totally new physics and enable unique functionality that can be exploited in the design of electrode materials [23,24]. Formation of heterostructures based on Gr and transition metal dichalcogenides (TMDCs) have been found to be especially attractive due to the wide range of properties they possess that can complement the shortcomings of Gr. Several theoretical studies have established that Gr hybrid with Hafnium disulfide (Gr/HfS_2) [3], Antimonene (Gr/Sb) [25], phosphorene (P/Gr) [26], as well as experimental synthesis of two-dimensional MXene/Gr heterostructures [27, 28], among others, have good performance in energy storage applications. In addition, vertical heterostructures have an interlayer distance that can be adjusted to intercalate more metal ions and further enhance the specific capacity of batteries [29].

Zr compounds have been found useful for thin film applications (ZrO_2) [30–32], electronic applications (ZrS_2 and $ZrSe_2$) among others. However, ZrS_2 and $ZrSe_2$ are the TMDC materials of interest in this work. Their compounds crystallize in a layered type structure. They have strong covalent bonds within the layers and weak van der Waals interaction between the layers [33]. They have the form TX_2 (where T is a transition metal and X is a chalcogen), all TMDCs have a hexagonal structure, with each monolayer comprising three stacked layers (X-T-X) [34]. ZrS_2 is a transparent semiconducting TMDC with an indirect band gap of 1.28 eV and an electron mobility of 1,200 $cm^2\ V^{-1}\ s^{-1}$ [7]. In addition it has an empty *d* valence band [35], good thermodynamic stability and is environmentally friendly [36]. Meanwhile, monolayer $ZrSe_2$ is a semiconductor with an indirect electronic band gap of ≈ 0.25 eV, and an electron mobility of 2,316 $cm^2 \bullet V^{-1} \bullet s^{-1}$ [8,9,37]. The layered structure of ZrS_2 and $ZrSe_2$ makes them excellent hosts for guest atom

* Corresponding author.
E-mail address: gking.kingori@gamil.com (G.W. King'ori).

https://doi.org/10.1016/j.surfin.2021.101036
Received 14 December 2020; Received in revised form 8 February 2021; Accepted 17 February 2021
Available online 23 February 2021

Table 1
Bulk lattice constants as calculated with vdW-DF2.

Material		a (Å)	c (Å)
	This work	2.46	3.35
Graphite	Experiment	2.46 [50]	3.36 [50, 51]
	Others theoretical studies	2.47 [52]	
	This work	3.68	5.98
ZrS_2	Experiment	3.66 ± 0.030 [53] 3.63 – 3.66 [54]	5.85 ± 0.030 [53] 5.81 – 5.85 [54]
	Others theoretical studies	3.687 [54]	6.659 [54], 6.32 [55]
	This work	3.76	6.13
$ZrSe_2$	Experiment	3.76 ± 0.010 [53] 3.77 – 3.80 [54]	6.15 ± 0.010 [53] 6.14 – 6.19 [54]
	Others theoretical studies	3.804 [56] 3.768 [54]	6.753 [56], 6.155 [54]

intercalation that can also tune their already novel properties [34, 38–40]. There are two possible polymorphs for monolayer TMDCs: 1T-phase with D3d point group and 2H-phase with D3h point group. The 2H-phases of Zr-compounds are dynamically unstable and therefore, we only focus on the 1T-phase of the TMDCs of interest [41,42]. In this work we investigated using density functional theory, vertically-stacked van der Waals heterostructures of Gr-ZrS_2 and Gr-$ZrSe_2$. The stacking configurations as well as the structural, electronic, electrochemical and intercalation properties of Gr-ZrS_2 and Gr-$ZrSe_2$ heterostructures, were explored.

2. Computational details

Density functional theory based calculations as implemented in Quantum ESPRESSO code [43] were used to investigate the various properties of the Gr-ZrX_2 heterostructures. In these calculations, a plane-wave basis set with an energy cut-off of 90 Ry was used. The study also used the Perdew–Burke–Ernzerhof (PBE) functional [44] for exchange-correlation approximation. In this study, ions-electrons interaction has been described using norm-conserving pseudopotentials [45] for all the atoms species. In addition, to account for the van der Waals interactions at the interface of the Gr-ZrS_2 and Gr-$ZrSe_2$ systems, the Van der Waals density functional (vdW-DF2) scheme [46] was employed in all the calculations. A 10^{-6} eV energy and a 10^{-3} eV $Å^{-1}$ force convergence criteria were set to achieve the ground state structure and its energy. A gamma centred 8 × 8 × 1 K-point mesh was used to sample the irreducible Brillouin zone of the heterostructures. All mentioned parameters were carefully examined to guarantee convergence in subsequent calculations (see Figure S1–Figure S3 in supplementary material). The respective monolayers to prepare the heterostructures were obtained from the optimized bulk structures of Gr and ZrX_2 (where X= S, Se). The monolayer unit cells of Gr and ZrX_2 were created from the bulk systems by adding a 20 Å vacuum along *c* axis. The atomic positions of the monolayer systems were relaxed keeping the volume fixed.

To reduce the lattice mismatch between the monolayers, the Gr-ZrX_2 heterostructure was constructed by considering different supercell sizes. In this case, a heterostructure with a 3 × 3 × 1 supercell of Gr and a 2 × 2 × 1 supercell of ZrX_2 were constructed, by stacking the Gr monolayer on top of the ZrX_2 monolayer. The resulting Gr-ZrX_2 heterostructure has 18 atoms of C, 8 atoms of X and 4 atoms of Zr. To determine the migration energy barrier for the diffusion of alkali Li and K intercalants, the climbing image nudged elastic band (CI-NEB) [47] method, as implemented in the Quantum ESPRESSO transition state tools was employed. The CI-NEB method with 3 - 5 images, depending on the length of the pathways, was used to calculate the minimum energy path (MEP) and the activation energy of alkali-ion diffusion. For comparison, alkali-ion diffusion through bilayer Gr (BLGr) and bilayer ZrX_2 ($BLZrS_2$) was also considered.

Table 2
Binding energies and lattice mismatches associated with the Gr-ZrX_2 heterostructure configurations. E_b is the binding energy per Carbon atom.

	E_b(eV)		Lattice mismatch	
	$GrZrS_2$	$GrZrSe_2$	$GrZrS_2$	$GrZrSe_2$
Gr as a reference	-0.80	-0.039	0.27 %	1.86 %
ZrX_2 as a reference	-0.07	-0.039	0.27 %	1.90 %
Gr and ZrX_2 as reference	-0.69	-0.038	0.14 %	0.94 %

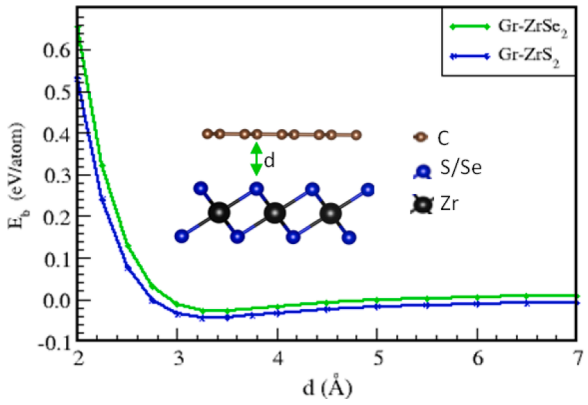

Figure 1. Optimized equilibrium interlayer distance of the Gr-ZrX_2 van der Waals heterostructure. Inset image shows the interlayer distance d of interest.

3. Results and discussion

3.1. Gr - ZrX_2 heterostructure stacking configurations

The Gr-ZrX_2 heterostructure is a vertical bilayer of Gr monolayer stacked on top of a ZrX_2 monolayer (see Figure 2), with a 20 Å vacuum also imposed on the heterostructure along the *c* axis. The calculated lattice parameters of the bulk systems are shown in Table 1 and compared to previous experimental and theoretical studies. To obtain the equilibrium stacking heterostructure configuration binding energy per C atom (E_b), of the different stacking configurations was obtained. The E_b was calculated using equation 1 [48,49].

$$E_b = \frac{E_{Gr-ZrX_2} - (E_{Gr} - E_{ZrX_2})}{N_C} \quad (1)$$

where, E_{Gr-ZrX_2}, E_{Gr} and E_{ZrX_2} are the calculated total energies of the Gr-ZrX_2 heterostructure, Gr monolayer and ZrX_2 monolayer respectively. N_c is the total number of C atoms in the heterostructure. The configuration with the lowest binding energy was chosen as the equilibrium heterostructure configuration to be used for subsequent calculations. The different stacking configurations considered, include; a configuration with the lattice parameter of Gr as the reference; a configuration with the lattice parameter(s) of ZrX_2 as reference; and a configuration with the lattice parameters of Gr and ZrX_2 averaged as reference. Table 2 shows the calculated E_b for the Gr-ZrX_2 heterostructures.

We note that the calculated binding energies are negative for all the systems investigated, confirming the stability of each system against phase separation. In addition, the binding energy indicates that the systems having Gr lattice parameter as the reference, are more stable than the rest as they had the lowest E_b. Using equation 2, the calculated lattice mismatch for the most stable Gr-ZrS_2 and Gr-$ZrSe_2$ heterostructures is 0.27 % and 1.86 % respectively. Both these values are within an acceptable range of mismatches used for heterostructures. Other systems have been found to exhibit higher mismatches of 1.37% for Gr/HfS_2 [3], 1.7% for Gr/Ti_2CO_2 [57], 1.7 % for Gr/hBN and 2.37% for HfS_2/$MoTe_2$ [58] heterostructures.

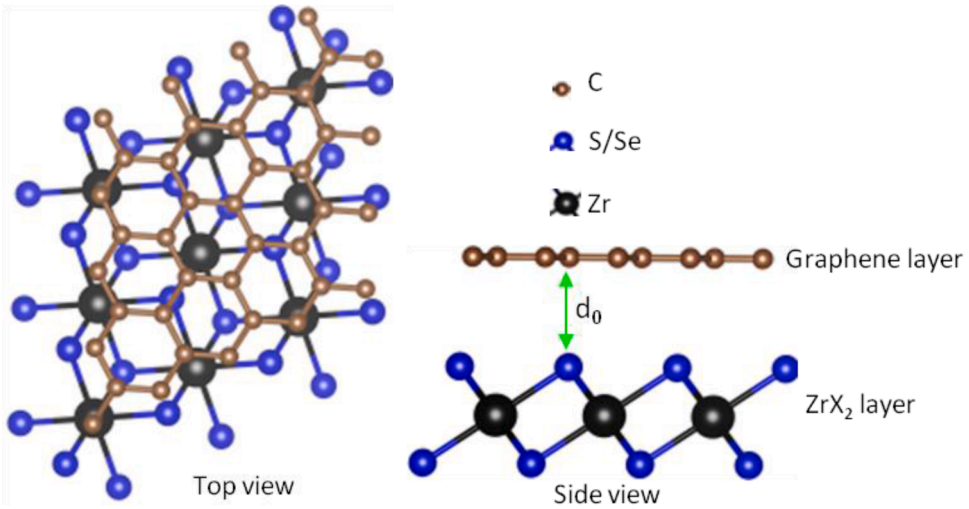

Figure 2. Top and side view of the optimized Gr-ZrX_2 heterostructure.

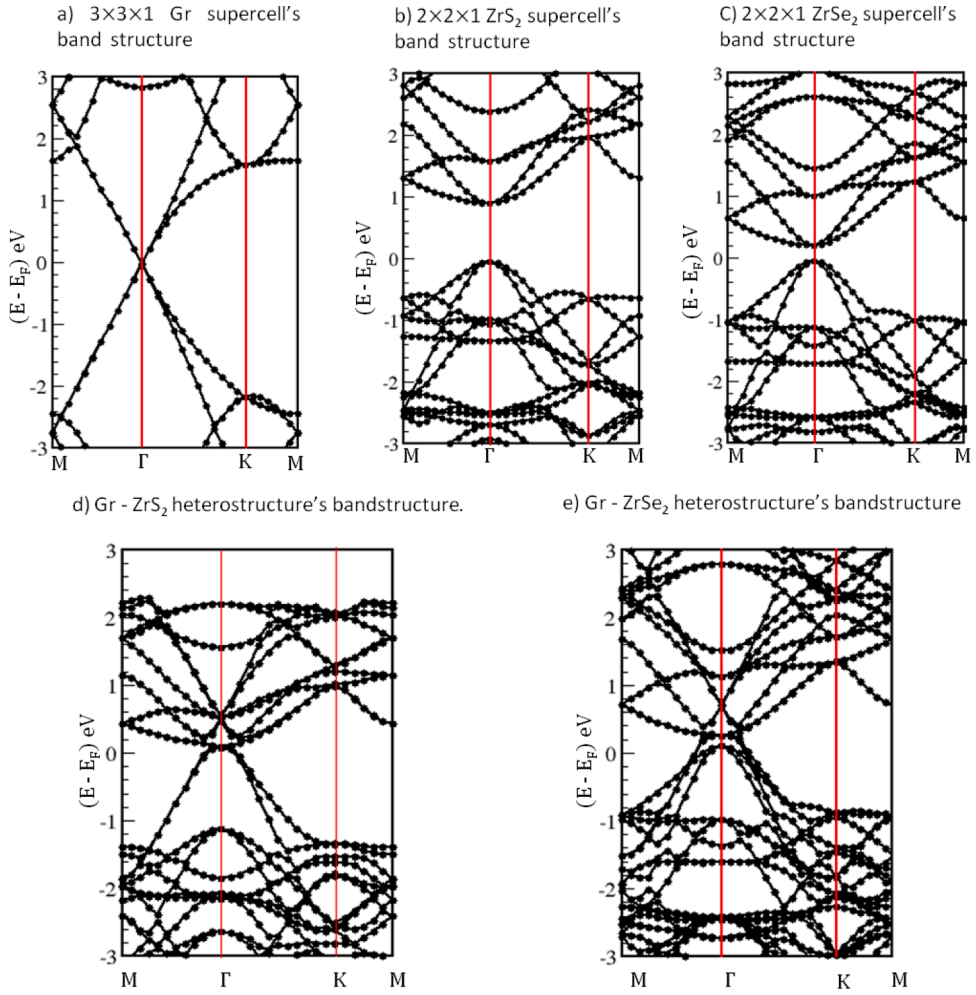

Figure 3. Calculated electronic band structures of the pristine (Gr, ZrS_2 & $ZrSe_2$) and heterostructure systems of Gr-ZrS_2 and Gr-$ZeSe_2$.

$$LM = \left|\frac{a_{L1} - a_{L2}}{a_{ref}}\right| \times 100\ \% \quad (2)$$

where a_{L1} and a_{L2} are the optimized lattice parameters of the first and second layers forming the heterostructure and a_{ref} is the lattice parameter of the layer used as reference.

E_b was further used to evaluate the interactions between the Gr monolayer and ZrX_2 monolayer forming the heterostructure, in order to obtain the equilibrium interlayer distance d_0 (see, Figure 1). The d value associated with the lowest value E_b (Figure 1) was chosen as the equilibrium inter layer distance, d_0.

The calculated d_0 for Gr-ZrS_2 and Gr-$ZrSe_2$ heterostructures was 3.25

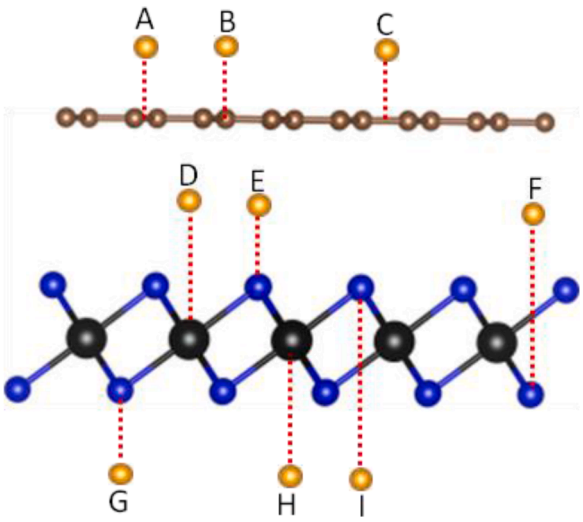

Figure 4. Adsorption/intercalation sites of the Li/K atom on the Gr-ZrX_2 vdW heterostructure.

Table 3
Adsorption energies (in eV) corresponding to alkali metal positioned in varying sites of the Gr-ZrX_2 heterostructure.

	Gr-ZrS_2		Gr-$ZrSe_2$	
Site	Li	K	Li	K
A	0.874	0.124	0.901	0.147
B	0.889	0.129	0.915	0.154
C	0.601	0.060	−0.034	0.089
D	−0.858	−0.939	−0.853	−0.876
E	−0.119	−0.528	−0.891	−0.880
F	−0.996	−1.000	−0.901	−0.890
G	0.220	−0.433	0.817	0.150
H	−0.707	−1.063	−0.170	−0.459
I	−0.881	−1.142	−0.230	−0.504

Å and 3.50 Å, respectively. These values were then used to obtain the equilibrium heterostructure geometry (configuration) of the form shown in Figure 2. This is what was used for all the subsequent calculations. The obtained interlayer distances indicate that the interlayer binding energy is stronger in Gr-ZrS_2 than in Gr-$ZrSe_2$, with the calculated values being −44.0 meV for Gr-ZrS_2 and −27.9 meV for Gr-$ZrSe_2$, respectively.

The calculated binding energies for Gr-ZrS_2 and Gr-$ZrSe_2$ heterostructures are consistent with what has been reported for Gr/h-BN heterostructure (-28 meV) [59] and Gr/Gr-like germanium carbide heterostructure (−38 meV) [60].

3.2. Electronic properties

The electronic band structures of the pristine monolayers and the proposed heterostructures are shown in Figure 3. As seen in Figure 3, Gr is semi metallic while the monolayer of ZrS_2 (see Figure 3b) has a band gap of 1.25 eV, which is consistent with a previous study that established its band gap to be 1.28 eV [35]. The $ZrSe_2$ monolayer (see Figure 3c) has an electronic band gap of 0.25 eV, which compares well with previous studies that have reported a band gap of 0.23 eV [37].

Both Gr-ZrS_2 and Gr-$ZrSe_2$ heterostructures were found to be metallic. This indicates that the presence of Gr improves the electronic conductivity of the pristine ZrX_2 monolayers. Other Gr based heterostructures with a metallic character include Gr /Tricyanomethanide (C_4N_3) [61] and SnO/Gr [62]. The lack of a bandgap in the Gr-ZrX_2 heterostructures, means that when used as electrode materials, the heterostructures would be expected to lead to efficient (seamless) movement of electrons in the electrode, hence enhancing conductivity.

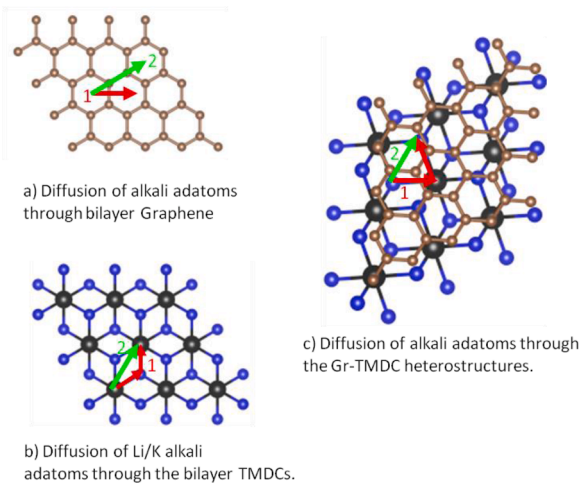

Figure 5. Minimum energy paths for the alkali metal intercalants

3.3. Alkali ion adsorption/intercalation

Intercalation/adsorption of ions into the heterostructure was done using only Li and K Intercalants. Na intercalation was not done since, borrowing from an earlier study, Na intercalation into Gr-HfS_2 [3] was found to be thermodynamically unstable. The optimal adsorption side for the alkali ions Li/K was identified by considering the alkali ion adsorbed above the Gr layer forming the heterostructure, in between the Gr and ZrX_2 layers and below the ZrX_2 layer. The adsorption sites considered are as shown in Figure 4 and their associated adsorption energies (E_a) (see Table 3) were calculated using equation 3,

$$E_a = \frac{(E_{GZrX_2-nM} - E_{GZrX_2} - nE_M)}{n} \quad (3)$$

where E_{GZrX_2-nM} is the total energy of the Gr-ZrX_2 heterostructure with

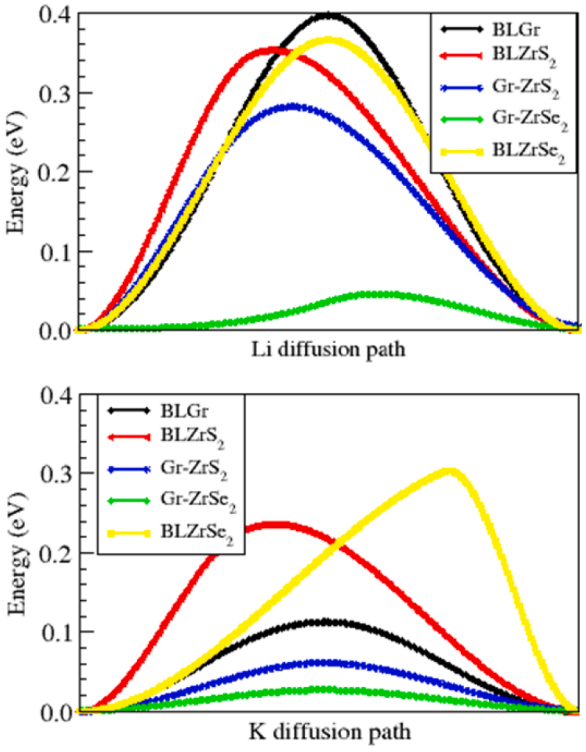

Figure 6. Energy profile associated with the paths shown in Figure 5. Only the lowest energy barrier profiles are shown for the various systems.

Table 4
Minimum energy barriers (in eV) associated with each intercalant through the various systems.

SYSTEM	Path	Li	K
Gr-ZrS_2	1	0.280	0.060
Gr-$ZrSe_2$	1	0.044	0.026
BLGr	1	0.390	0.110
$BLZrS_2$	1	0.350	0.110
$BLZrSe_2$	1	0.367	0.304

the alkali adatom, E_{GZrX_2} is the total energy of the Gr-ZrX_2 heterostructure without any adatom, E_M is the total energy of the free metal adatom, n corresponds to the number of alkali ions in the heterostructure, and M is the free metal adatom.

The F site in Figure 4 was the most energetically favoured intercalation site over the other sites considered for Li in Gr-ZrS_2, Gr-$ZrSe_2$ and K in Gr-$ZrSe_2$. Intercalation sites D and E were also favoured since the binding energies were also negative, it is worth noting that site I was favoured by K in Gr-ZrS_2. These E_a results indicate the possibility of alkali ion intercalations and alkalisation (lithiation) of the heterostructure. Sites A and B were not favoured by alkali ions in both Gr-ZrS_2 and Gr-$ZrSe_2$ heterostructures with site C also not favoured in the case of Gr-ZrS_2 heterostructure.

3.4. Diffusion of alkali ions

Having established that the Gr-ZrX_2 heterostructures enable electrical conductivity (see Figure 3), their ionic conductivity was investigated. The charge/discharge rates of metal-ion batteries predominantly depend on the ion diffusion within the electrode. Poor diffusivity leads to significant structural damage with continued cycling, consequently affecting the lifetime of the battery [63]. In order to estimate the feasibility of alkali metal intercalation in the heterostructures, an investigation of the migration of alkali ions is crucial. As indicated in the computational details, CI-NEB calculations were carried out to obtain the respective minimum energy paths (MEPs) (see Figure 5), and activation energies (see Figure 6). The activation energy, the energy difference between the highest energy point on the MEP and the reference point are given in Table 4. In all cases the K intercalant exhibits a lower activation energy than Li intercalant, a similar observation has been reported for 2D B_2P_6 [64] and for K intercalation in α- and β-beryllene [65]. Path 1 is also seen to be the preferred diffusion path in all the cases, diffusion of alkali ions preferring the zigzag path has also been reported VS_2 [66]. It is also worth noting from Table 4, that the minimum energy paths for the heterostructures have activation energies that are less than those of the pristine bilayers, indicating that formation of the heterostructures reduced the energy barriers associated with the pristine bilayers.

In addition, the activation energy barrier is significantly lower in the Gr-$ZrSe_2$ heterostructure than in the Gr-ZrS_2 in all the cases. This can be attributed to the difference in equilibrium interlayer distance between the heterostructures (3.25 Å and 3.50 Å for Gr-ZrS_2 and Gr-$ZrSe_2$ heterostructures, respectively). The larger interlayer distance in the $GrZrSe_2$ makes movement of intercalants in $GrZrSe_2$ easier than in Gr-ZrS_2. In general, the values of the activation energies associated with the heterostructures are lower than for Li ion on graphite (0.42 eV) [67] and that on commercially used anode materials based on TiO_2 (0.32−0.55eV) [68]. The lower alkali ion diffusion energy barriers in the heterostructure systems, imply faster kinetics for the battery operations, and hence improved battery rate performance for the heterostructures.

3.5. Electrochemical properties of the heterostructures

Ions usually intercalate into or deintercalate from the interlayer spaces of the heterostructure during charge or discharge cycles of batteries. To determine the intercalation properties of the heterostructure, Li/K adatoms were intercalated into the most favorable intercalation site followed by other equivalent sites one at a time. In each case, the atomic positions were relaxed fully to the required convergence threshold before addition of the next adatom. For each intercalant added, E_a was determined using equation 3. A plot of the binding energy per atom against the number of intercalated adatoms is shown in Figure 7. A strong binding between the Li/K intercalants and the host Gr-ZrX_2 bilayer is necessary to avoid the formation of metallic clusters, which improves the safety and reversibility of the alkali ion battery. We observe from Figure 7 that both heterostructures had binding energies that lie between the two extremes (BLGr < Gr-ZrS_2 < $BLZrX_2$). In addition, K intercalation into BLGr becomes endothermic at the point when a second K intercalant is positioned (see Figure 7 (b)). However, the heterostructures are able to take in intercalants in all the 4 symmetric equivalent sites. This indicates that the formation of the heterostructure moderates the binding energies associated with the pristine materials.

Another key aspect that determines the performance of an electrode is the open-circuit voltage (OCV). Negative values of the potential difference suggest that guest adatoms prefer to form metallic clusters

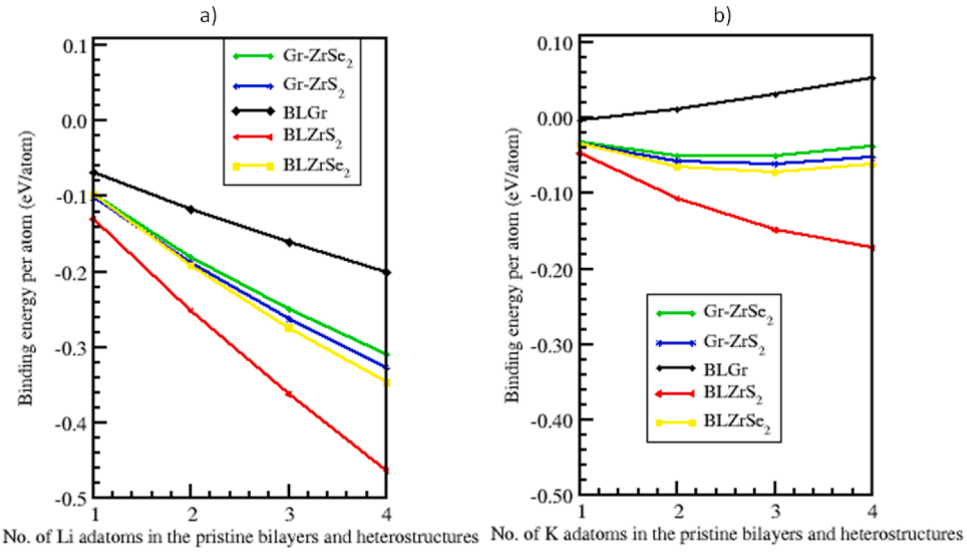

Figure 7. Average binding energy per atom in the structure as a function of the of intercalated Li/K adatoms

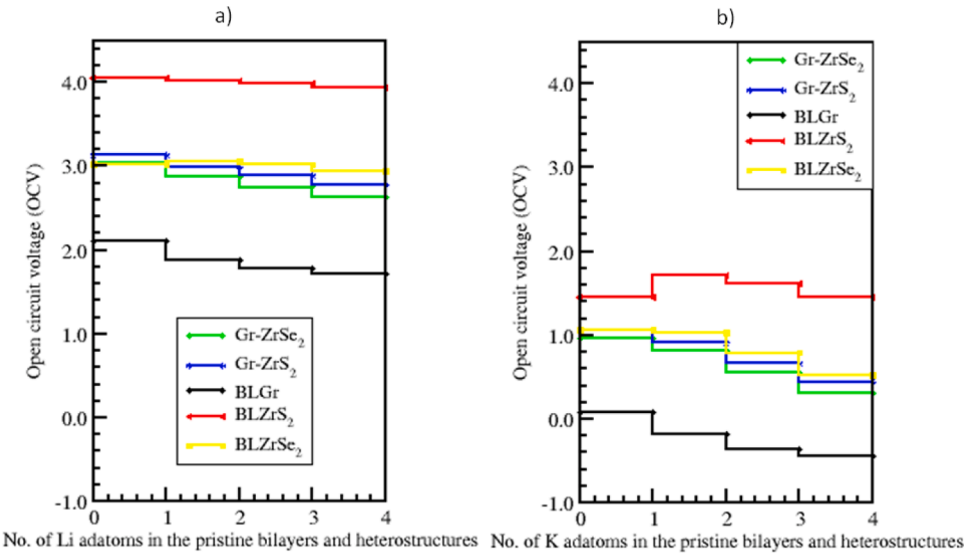

Figure 8. Open circuit voltage profiles as a function of Li/K concentration.

Table 5
Average OCV values (in V), associated with the pristine bilayers and the heterostructures.

System	Li-intercalated	K-intercalated
Gr-$ZrSe_2$	2.83	0.66
Gr-ZrS_2	2.95	0.77
BLGr	1.87	0.09
$BLZrS_2$	4.00	1.56
$BLZrSe_2$	3.01	0.80

Table 6
Specific capacity in mAh/g for different Li/K-Gr-ZrX_2 heterostructures.

System	Li	K
Gr-ZrS_2	480	448
Gr-$ZrSe_2$	640	243
Graphite	372 [74]	
Gr/Antimonene (Gr-Sb)	369.03 [25]	
Gr/Vanadium disulfide (Gr-VS_2)	569 [6]	
Germanium selenide/black phosphorus (GeSe/BP)		313.67 [75]

instead of adsorption to the electrode, while positive values indicate intercalation possibility. In order to gain insights into the changes that occur in the process of Li and K intercalation into the Gr-ZrX_2 heterostructures, the open-circuit-voltage (OCV) was determined using equation 4 [69–71].

$$V \approx \frac{[(E_{GrZrS_2+x_{1M}} - E_{GrZrS_2+x_{2M}}) + (x_{2-} x_1)\mu_M]}{(x_{2-} x_1)\, e} \quad (4)$$

where $E_{GrZrS_2+x_{1M}}$ and $E_{GrZrS_2+x_{2M}}$ are the total energies of the Gr-ZrX_2 heterostructure with x_1 and x_2 alkali adatom intercalated, respectively, μ_M is the chemical potential of Li/K atom and e denotes the elementary charge quantity. The chemical potential of Li/K atom is approximately equal to the total energy per Li/K adatom, and hence this was the value used in equation 4 [69,71]. For comparison purposes, the OCV for the bilayer materials was also considered. The calculated voltage profiles are shown in Figure 8. It is observed that the voltage decreases gradually, except for Li-$BLZrSe_2$ and K-$BLZrS_2$, whose OCV initially increases after insertion of the first intercalant and then decreases. This is indicative of a stable voltage for the intercalated adatoms; and this further suggests good cycling performance [72]. As seen in Figure 8, except for the profile associated with K-BLGr, all the other systems have a positive value even after intercalating all the identical most favoured sites, indicating that additional adatoms can be intercalated by seeking other less favourable sites. The calculated voltage values correlate with the binding energy values, whereby the highest voltage is found for Li intercalated $BLZrS_2$, since this system has the largest binding energy (see Figure 7 (a)).

The calculated OCVs are shown in Table 5. It is observed that the calculated voltage values correlate with the binding energy values per atom (see Figure 7). Li intercalated systems have higher binding energy values and hence higher OCV, than K intercalated systems. Since ideally, a good anode should have a low electrode potential, our calculated voltage profile suggest that the K intercalated systems with average OCV of less than 1.56 V are suitable as anodes for Lithium Ion batteries. For the heterostructures the average OCV values are 0.66 V, 0.77 V and 0.80 V for K intercalated $GrZrSe_2$, $GrZrS_2$ and $BLZrSe_2$, respectively, and these values are within the desired potential range (0.10 –1.00 V) for anode materials [69]. These systems would therefore, be suitable for use as anode materials in Potassium Ion Batteries (KIBs). In the case of Li intercalated systems, except for BLGr, the other systems have OCV's ranging between 2.83 - 4.00 V and hence would be more suitable for use as cathode materials for LIBs.

Theoretical specific capacity is another important electrode property, that describes the maximum number of Li/K adatoms that could be intercalated in the heterostructures. This was determined by seeking all the favourable intercalation sites in the heterostructures. For each adatom added, the adsorption energy was determined using equation 3, up to the point where the reaction becomes endothermic. This point marks the capacity limit for the given electrode material. The theoretical specific capacity of the heterostructures for various species was then determined from equation 5 [73];

$$C = \frac{xN_A n_e e}{m} \quad (5)$$

where C refers to the specific capacity of the heterostructure, x is the maximum number of intercalated ions in the electrode, N_A is the Avogadro constant, n_e is the valence of ions, e is the electric charge of an electron, m is the molar mass of the heterostructure with ion intercalation. The reaction at the anode for the graphene-ZrX_2 heterostructure can be expressed as shown in equation 6 [72];

$$xLiC_{18}/(ZrX_2)_4 \rightleftarrows xLi^+ + xe^- + C_{18}/(ZrX_2)_4 \quad (6)$$

where x is the maximum number of intercalated ions in the heterostructure, e is the electric charge of an electron, C_{18} refers to the atoms in

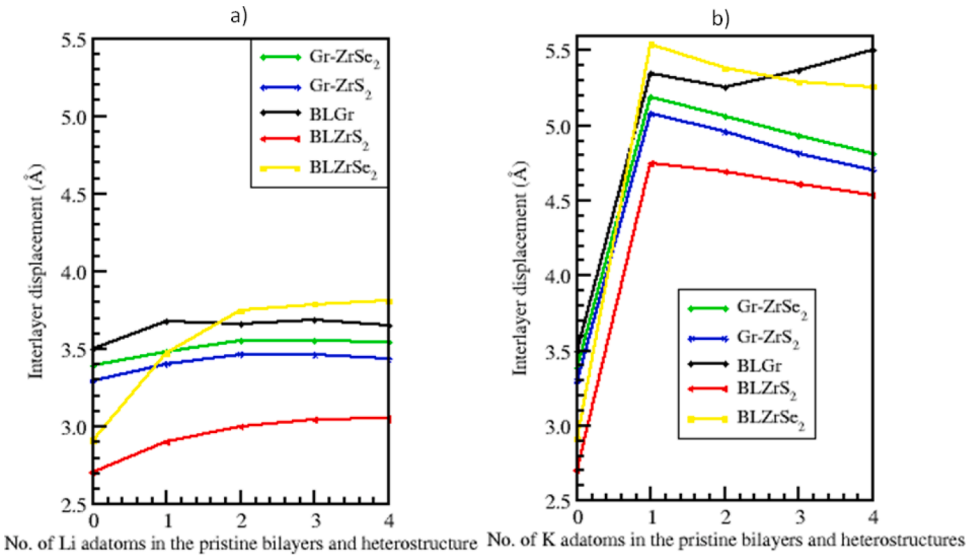

Figure 9. The interlayer displacement as a function of intercalated alkali adatoms.

Table 7
Maximum volumetric expansion in the z-direction associated with the pristine bilayers and the heterostructures

System	Li-intercalated	K-intercalated
Gr-$ZrSe_2$	4.85 %	53.07 %
Gr-ZrS_2	5.19 %	54.13 %
BLG	5.28 %	57.17 %
$BLZrS_2$	30.86 %	75.61 %
$BLZrSe_2$	12.73 %	90.32 %

the Gr layer and $(ZrX_2)_4$ refers to the size of the TMDC layer.

The maximum number of Li and K intercalants that could be intercalated in the heterostructure layers, gives a theoretical specific capacity of the Gr-ZrX_2 heterostructures as shown in Table 6. The table also includes a comparison with other Gr based heterostructures that have been proposed as suitable electrode materials.

Li intercalated Gr-$ZrSe_2$ heterostructure has the highest theoretical specific capacity while K intercalated Gr-$ZrSe_2$ heterostructure has the least. Except for the K intercalated Gr-$ZrSe_2$ heterostructure, the theoretical capacity for the other three systems is higher than the one for commercially used graphite which is 372 mAh/g [74]. The calculated theoretical capacities suggests that the intercalated Gr-ZrX_2 heterostructures are indeed suitable as anode materials for both LIB and KIB. As seen from Figure S4 (in the supplementary material), Li intercalated Gr-$ZrSe_2$ is still in a position to accommodate many more intercalants, since even at 29 intercalants, it has not attained its maximum adsorption energy per atom.

3.6. *Influence of alkali adatom intercalation on interlayer distance*

A good electrode material for rechargeable ion batteries should be one with small volume evolution upon intercalating ions. The change in the interlayer distance between the two layers forming the Gr-ZrX_2 heterostructure as a function of the intercalated Li/K adatoms is shown in Figure 9. The maximum volumetric expansion in the *z*-direction associated with each system is shown in Table 7. It is observed that for each intercalant, the maximum volume expansion is evident in the pristine materials, while the heterostructures moderate these expansion. Except for the K intercalated BLGr, the other systems after peaking at 1 K intercalant, undergo a reduction in interlayer spacing (see Figure 9 (b)). The maximum volumetric expansion associated with the Gr-$ZrSe_2$ (Gr-ZrS_2) heterostructures is respectively, 4.85 (5.19) % and 53.07 (54.13) % for Li and K intercalants. The Gr-$ZrSe_2$ has a lower volume expansion than Gr-ZrS_2. However, these volumetric expansions are comparable to that for K intercalation in graphite (~61 %) [76] or Li intercalation in graphite anodes (10%) [77], and much lower than for silicon based electrodes which is 280% [78] or 260% for alloy-type anodes of Germanium (Ge) and Tin (Sn), and 300% for Phosphorus (P) [77].

The combination of positive and negative volume changes observed during intercalation into the heterostructures, can help maintain the structural integrity of the Gr-ZrX_2 heterostructure during the discharge/charge process. This could mean that Gr-ZrX_2 heterostructure is likely to possess a reversible reaction process of Li and K adatoms intercalation.

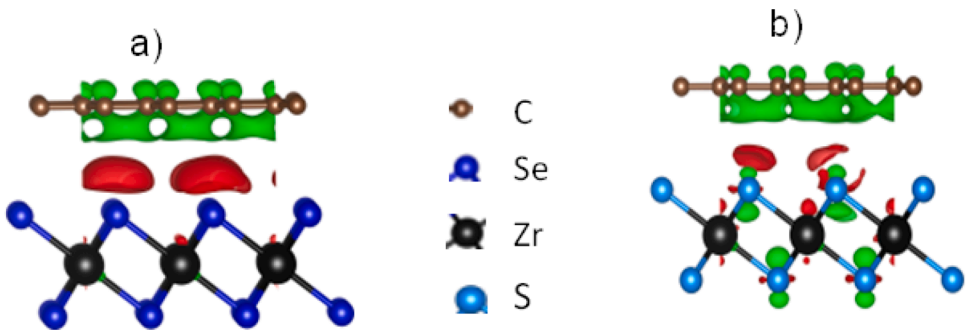

Figure 10. Charge density difference plots for the (a) Gr-$ZrSe_2$ and (b) Gr-ZrS_2 heterostructure systems

Table 8
Lowdin charge difference associated with varying levels of Li intercalation in the Gr-ZrX_2 hosts.

	Gr-ZrS_2				Gr-$ZrSe_2$			
No. of intercalants	Zr	S_2	C	Li	Zr	Se_2	C	Li
1 Li	-0.023	-0.005	0.006	3.032	-0.031	0.011	0.005	3.029
2 Li	-0.033	0.009	0.011	2.991	-0.039	0.027	0.010	2.970
3 Li	-0.058	0.024	0.022	2.950	-0.063	0.043	0.023	2.925
4 Li	-0.069	0.049	0.031	2.916	-0.064	0.075	0.030	2.166

Table 9
Lowdin charge difference associated with varying levels of K intercalation in the Gr-ZrX_2 hosts.

	Gr-ZrS_2				Gr-$ZrSe_2$			
No. of intercalants	Zr	S_2	C	K	Zr	Se_2	C	K
1 K	-0.008	-0.047	0.017	8.939	-0.008	-0.035	0.019	8.830
2 K	-0.017	-0.049	0.025	8.944	-0.020	-0.028	0.025	8.898
3 K	-0.030	-0.056	0.029	8.976	-0.031	-0.025	0.031	8.920
4 K	-0.032	0.053	0.028	8.997	-0.024	-0.012	0.027	8.945

3.7. Charge density distribution

To visualize the charge transfer from either Li/K to the Gr-ZrX_2 host, the charge density iso-surface plots were evaluated for the most favoured intercalation sites, using the charge densities difference ($\Delta\rho$) relation given by equation 7:

$$\Delta\rho = \Delta\rho_{Gr-ZrX_2+nM} - \Delta\rho_{Gr-Zr_2} - \Delta\rho_{nM} \quad (7)$$

where ρ_{Gr-ZrX_2+nM} is the charge density of the heterostructure with adatom, $\Delta\ \rho_{Gr-ZrX_2}$ is the charge density of the heterostructure and $\Delta\rho_{nM}$ is the charge density of n number of Li/K adatoms. M is the free metal adatom. The resulting charge density difference distribution is shown in Figure S5–Figure S8, in the supplementary material. Charge accumulation is shown by the red iso-surface while charge depletion is represented by the green iso-surface. In addition, the iso-surface level for the pristine Gr-ZrX_2 heterostructure is found to be 0.001 e/Å^3 while that of the intercalated heterostructures is 0.003 e/Å^3. Before introduction of the intercalant (see Figure 10), the Gr layer is observed to be a region of charge depletion while that around the ZrX_2 layer has charge accumulation.

Upon intercalation, the intercalants induce charge transfer in which case the intercalants donate their charges to the host, leaving them depleted of charge, while the Gr layer is observed to receive most of the donated charges and becomes an isosurface of charge accumulation (see Figure S5–Figure S8 in the supplementary material). The ZrX_2 surface also receives a substantial amount of charge and hence becomes an isosurface of charge accumulation. This observation is further confirmed by the results of the Lowdin charge difference shown in Table 8 and Table 9.

The alkali intercalants gain a positive charge upon adsorption into the heterostructure. Similar observations have been made previously for the Gr/MoS_2 [79] and tungsten sulphide Ws_2/Gr [80] heterostructures. It has also been shown that Tungsten diselenide (WSe_2) is a weak acceptor of electrons upon contact with Gr, in a WSe_2/Gr heterostructure [81]. Charge transfer to the host system is known to increase the value of the binding energy as it gives rise to stronger ionic interactions [82], which explains the increase in binding energy that is observed for the heterostructure, (see Figure 7).

4. Conclusion

In this work, we combined the outstanding electrical conductivity of Gr with the unique crystal structure of ZrX_2 to construct vertical bilayer Gr-ZrX_2 heterostructures. We carried out first-principles calculations to systematically explore their feasibility as electrode materials for alkali-ion batteries. The ground state stable stacking configurations of Gr-ZrX_2 bilayer heterostructures was determined as the configuration that uses the Gr lattice parameters as the reference parameters for the heterostructure. For the ground state stacking, the interlayer binding is strong, and was found to decrease as the Li/K concentration increases due to enhanced repulsive interaction between the positively charged Li/K ions. The Li/K intercalated Gr-ZrX_2 heterostructure was found to exhibits large atom binding energies, thus making it a promising candidate for battery applications. In addition, intercalant diffusion in the heterostructures is associated with lower energy barrier heights, which imply faster kinetics for the battery operations. The results of this study also show that formation of the heterostructures improves the intercalation properties of the pristine bilayers. The findings of this study suggest that the layered Gr-ZrX_2 heterostructures have the advantage of good electrical and ionic conductivity, appropriate open circuit voltage, high theoretical specific capacities and moderate volume expansion, all of which are essential for proper operation of a battery.

Sample CRediT author statement

Gladys W. King'ori: Conceptualization, Investigation, Formal analysis, Writing - original draft, Review & editing; **Cecil N M Ouma:** Conceptualization, Project administration, Supervision, analysis and/or interpretation of data; **George O. Amolo:** Supervision, analysis and/or interpretation of data; **Nicholas W. Makau:** Supervision, analysis and/or interpretation of data.

Declaration of Competing Interest

The authors declare that they have no known competing financial interests or personal relationships that could have appeared to influence the work reported in this paper.

Acknowledgements

The authors wish to acknowledge the computer resources, technical expertise, and assistance provided by the Centre for High Performance Computing (CHPC-MATS862), Cape Town, South Africa, in carrying out this work.

Supplementary materials

Supplementary material associated with this article can be found, in the online version, at doi:10.1016/j.surfin.2021.101036.

References

[1] W. Zhang, Y. Liu, Z. Guo, Approaching high-performance potassium-ion batteries via advanced design strategies and engineering, Sci. Adv. 5 (5) (2019) 1–13.
[2] N. Mohamed, N.K. Allam, Recent advances in the design of cathode materials for Li-ion batteries, RSC Adv 10 (37) (2020) 21662–21685.
[3] G.W. King'ori, C.N.M. Ouma, A.K. Mishra, G.O. Amolo, N.W. Makau, Two-dimensional graphene–HfS_2 van der Waals heterostructure as electrode material for alkali-ion batteries, RSC Adv 10 (2020) 30127–30138.
[4] M. Gmitra, J. Fabian, Graphene on transition-metal dichalcogenides: A platform for proximity spin-orbit physics and optospintronics, Phys. Rev. B - Condens. Matter Mater. Phys. 92 (15) (Oct. 2015) 1–6.
[5] S.-J. Liang, B. Liu, W. Hu, K. Zhou, L.K. Ang, Thermionic Energy Conversion Based on Graphene van der Waals Heterostructures, Sci. Rep. 7 (2017) 1–7.
[6] N.S. Mikhaleva, M.A. Visotin, A.A. Kuzubov, Z.I. Popov, VS_2 /Graphene Heterostructures as Promising Anode Material for Li-Ion Batteries, J. Phys. Chem. C 121 (43) (Nov. 2017) 24179–24184.
[7] M. Hamada, et al., High Hall-Effect Mobility of Large-Area Atomic-Layered Polycrystalline ZrS_2 Film Using UHV RF Magnetron Sputtering and Sulfurization, IEEE J. Electron Devices Soc. 7 (2019) 1258–1263.
[8] W. Zhang, Z. Huang, W. Zhang, Y. Li, Two-dimensional semiconductors with possible high room temperature mobility, Nano Res 7 (12) (2014) 1731–1737.
[9] M. Zhang, et al., Controlled Synthesis of ZrS_2 Monolayer and Few Layers on Hexagonal Boron Nitride, J. Am. Chem. Soc. 137 (22) (2015) 7051–7054.
[10] K.O. Obodo, G. Gebreyesus, C.N.M. Ouma, Controlling the electronic and optical properties of HfS_2 mono-layers via lanthanide substitutional doping: a DFT+U study, RSC Adv. (2020) 15670–15676.
[11] U.S. Sun. Minglei, δ-CS: A Direct-Band-Gap Semiconductor Combining Auxeticity, Ferroelasticity, and Potential for High-Efficiency Solar Cells, Phys. Rev. Appl. 14 (4) (2020) 044015–044020.
[12] M. Sun, J.P. Chou, A. Hu, U. Schwingenschlögl, Point Defects in Blue Phosphorene, Chem. Mater. 31 (19) (2019) 8129–8135.
[13] K. Onyebuchi, C. Naphtaly, M. Ouma, J. Tobechukwu, M. Braun, D. Bessarabov, Computational Condensed Matter First principles study of single and multi-site transition metal dopant ions in MoS_2 monolayer, Comput. Condens. Matter 21 (2019) 1–7.
[14] S. Wang, M.S. Ukhtary, R. Saito, Strain effect on circularly polarized electroluminescence in transition metal dichalcogenides, Phys. Rev. Res. 2 (3) (2020) 033340–033346.
[15] C.H. Lee, et al., Tungsten Ditelluride: A layered semimetal, Sci. Rep. 5 (2015) 1–8.
[16] B. Yan, et al., Broadband 1T-titanium selenide-based saturable absorbers for solid-state bulk lasers, Nanoscale 10 (43) (2018) 20171–20177.
[17] J. Zhu, H.N. Alshareef, U. Schwingenschlögl, Functionalized NbS_2 as cathode for Li- and Na-ion batteries, Appl. Phys. Lett. 111 (2017) 043903–043908.
[18] F. Ming, H. Liang, Y. Lei, W. Zhang, H.N. Alshareef, Solution synthesis of VSe_2 nanosheets and their alkali metal ion storage performance, Nano Energy 53 (2018) 11–16.
[19] T.P. Kaloni, S. Mukherjee, Comparative study of electronic properties of graphite and hexagonal boron nitride (h-BN) using pseudopotential plane wave method, Mod. Phys. Lett. B 25 (2011) 1855–1866.
[20] V.V. Ivanovskaya, A.N. Enyashin, N.I. Medvedeva, A.L. Ivanovskii, Electronic properties of superconducting $NbSe_2$ nanotubes, Phys. Status Solidi Basic Res. 238 (2003) 2–5.
[21] N.F. Hinsche, K.S. Thygesen, Electron-phonon interaction and transport properties of metallic bulk and monolayer transition metal dichalcogenide TaS_2, 2D Mater. 5 (2018) 1–7.
[22] S. Wang, C. Ren, H. Tian, J. Yu, M. Sun, MoS2/ZnO van der Waals heterostructure as a high-efficiency water splitting photocatalyst: A first-principles study, Phys. Chem. Chem. Phys. 20 (2018) 13394–13399.
[23] W. Ren, H.M. Cheng, The global growth of graphene, Nat. Nanotechnol. 9 (10) (2014) 726–730.
[24] Q. Ke, J. Wang, Graphene-based materials for supercapacitor electrodes – A review, J. Mater. 2 (2016) 37–54.
[25] P. Wu, P. Li, M. Huang, Potential application of graphene/antimonene herterostructure as an anode for Li-ion batteries: A first-principles study, Nanomaterials 9 (2019) 1–16.
[26] X. G., L.H. Linxia Wang, Zhiqiang Jiang, Wei Li, Hybrid phosphorene /graphene nanocomposite as an anode material for Na-ion batteries : a first-principles study, J. Phys. D. Appl. Phys. 50 (2017) 1–7.
[27] Q. Yang, et al., MXene/graphene hybrid fibers for high performance flexible supercapacitors, J. Mater. Chem. A 5 (42) (2017) 22113–22119.
[28] J. Yan, et al., Flexible MXene/Graphene Films for Ultrafast Supercapacitors with Outstanding Volumetric Capacitance, Adv. Funct. Mater. 27 (2017) 1–10.
[29] E.M.D. Siriwardane, I. Demiroglu, C. Sevik, D. Çaklr, Achieving Fast Kinetics and Enhanced Li Storage Capacity for $Ti_3C_2O_2$ by Intercalation of Quinone Molecules, ACS Appl. Energy Mater. 2 (2019) 1251–1258.
[30] W. He, et al., Surface Modification on Solution Processable ZrO_2 High-k Dielectrics for Low Voltage Operations of Organic Thin Film Transistors, J. Phys. Chem. C 120 (2016) 9949–9957.
[31] Y. Gong, et al., Solution processable high quality ZrO_2 dielectric films for low operation voltage and flexible organic thin film transistor applications, J. Phys. D. Appl. Phys. 51 (2018) 1–9.
[32] Y. Gong, et al., Room Temperature Fabrication of High Quality ZrO_2 Dielectric Films for High Performance Flexible Organic Transistor Applications, IEEE Electron Device Lett 39 (2018) 280–283.
[33] G.H. Han, D.L. Duong, D.H. Keum, S.J. Yun, Y.H. Lee, Van der Waals Metallic Transition Metal Dichalcogenides, Chem. Rev. 118 (2018) 6297–6336.
[34] K.S. Novoselov, A. Mishchenko, A. Carvalho, A.H. Castro Neto, 2D materials and van der Waals heterostructures, Science (80) 353 (2016) 461–473.
[35] T.V. Vu, et al., Electronic properties and optical behaviors of bulk and monolayer ZrS_2: A theoretical investigation, Superlattices Microstruct 125 (2019) 205–213.
[36] Y. Si, et al., Dramatically Enhanced Visible Light Response of Monolayer ZrS2 via Non-covalent Modification by Double-Ring Tubular B_20 Cluster, Nanoscale Res. Lett. 11 (2016) 1–7.
[37] F.A. Rasmussen, K.S. Thygesen, Computational 2D Materials Database: Electronic Structure of Transition-Metal Dichalcogenides and Oxides, J. Phys. Chem. C 119 (2015) 13169–13183.
[38] N. Glebko, I. Aleksandrova, G.C. Tewari, T.S. Tripathi, M. Karppinen, A. J. Karttunen, Electronic and Vibrational Properties of TiS_2, ZrS_2, and HfS_2: Periodic Trends Studied by Dispersion-Corrected Hybrid Density Functional Methods, J. Phys. Chem. C 122 (2018) 26835–26844.
[39] Z. Zhang, P. Lin, Q. Liao, Z. Kang, H. Si, Y. Zhang, Graphene-Based Mixed-Dimensional van der Waals Heterostructures for Advanced Optoelectronics, Adv. Mater. 31 (37) (2019) 1–15.
[40] C. Yan, et al., 2D Group IVB Transition Metal Dichalcogenides, Adv. Funct. Mater. 28 (2018) 1–18.
[41] C. Cheng, J.T. Sun, X.R. Chen, S. Meng, Hidden spin polarization in the 1T-phase layered transition-metal dichalcogenides MX_2 (M = Zr, Hf; X = S, Se, Te), Sci. Bull. 63 (2) (2018) 85–91.
[42] S.U. Rehman, Z.J. Ding, Enhanced electronic and optical properties of three TMD heterobilayers, Phys. Chem. Chem. Phys. 20 (24) (2018) 16604–16614.
[43] P. Giannozzi, et al., QUANTUM ESPRESSO: A modular and open-source software project for quantum simulations of materials, J. Phys. Condens. Matter 21 (39) (Sep. 2009), 395502.
[44] X. Xu, W.A. Goddard, The extended Perdew-Burke-Ernzerhof functional with improved accuracy for thermodynamic and electronic properties of molecular systems, J. Chem. Phys. 121 (9) (2004) 4068–4082.
[45] D.R. Hamann, M. Schlüter, C. Chiang, Norm-Conserving Pseudopotentials, Phys. Rev. Lett. 43 (20) (1979) 1494–1497.
[46] K. Berland, et al., van der Waals forces in density functional theory: a review of the vdW-DF method, Rep. Prog. Phys. 78 (6) (2015) 1–41.
[47] G. Henkelman, B.P. Uberuaga, H. Jónsson, Climbing image nudged elastic band method for finding saddle points and minimum energy paths, J. Chem. Phys. 113 (2000) 9901–9904.
[48] C.N.M. Ouma, K.O. Obodo, M. Braun, G.O. Amolo, Ab initio insights on the effect of embedding lanthanide atoms on nitrogenated holey doped graphene (g-C_2N), J. Mater. Chem. C 6 (2018) 4015–4022.
[49] K.O. Obodo, C.N.M. Ouma, J.T. Obodo, M. Braun, Influence of transition metal doping on the electronic and optical properties of ReS_2 and $ReSe_2$ monolayers, Phys. Chem. Chem. Phys. 19 (2017) 19050–19057.
[50] L.A. Girifalco, R.A. Lad, Energy of cohesion, compressibility, and the potential energy functions of the graphite system, J. Chem. Phys. 25 (1956) 693–697.
[51] L.X. Benedict, N.G. Chopra, M.L. Cohen, A. Zettl, S.G. Louie, V.H. Crespi, Microscopic determination of the interlayer binding energy in graphite, Chem. Phys. Lett. 286 (1998) 490–496.
[52] J. Wang, F. Ma, M. Sun, Graphene, hexagonal boron nitride, and their heterostructures: properties and applications, RSC Adv 7 (2017) 16801–16822.
[53] D.L. Greenaway, R. Nitsche, Preparation and optical properties of group IV–VI2 chalcogenides having the CdI_2 structure, J. Phys. Chem. Solids 26 (1965) 1445–1459.
[54] S.M. Oliver, H.-P.K. Joshua J. Fox, Arsalan Hashemi, Akshay Singh, Randal L. Cavalero, Sam Yee, David W. Snyder, R. Jaramillo, P.M. Vora, Phonons and Excitons in $ZrSe_2$ - ZrS_2 Alloys, J. Mater. Chem. C 8 (2020) 5732–5743.
[55] Q. Zhao, Y. Guo, K. Si, Z. Ren, J. Bai, X. Xu, Elastic, electronic, and dielectric properties of bulk and monolayer ZrS_2, $ZrSe_2$, HfS_2, $HfSe_2$ from van der Waals density-functional theory, Phys. Status Solidi B 254 (2017) 119–120.
[56] H. Jiang, Structural and electronic properties of ZrX_2 and HfX_2 (X = S and Se) from first principles calculations, J. Chem. Phys. 134 (2011) 1–9.
[57] Y.T. Du, X. Kan, F. Yang, L.Y. Gan, U. Schwingenschlögl, MXene/Graphene Heterostructures as High-Performance Electrodes for Li-Ion Batteries, ACS Appl. Mater. Interfaces 10 (2018) 32867–32873.
[58] X. Yang, et al., HfS_2/$MoTe_2$ vdW heterostructure: Bandstructure and strain engineering based on first-principles calculation, RSC Adv 10 (2020) 2615–2623.
[59] I. Leven, T. Maaravi, I. Azuri, L. Kronik, O. Hod, Interlayer Potential for Graphene/h-BN Heterostructures, J. Chem. Theory Comput. 12 (2016) 2896–2905.
[60] S. Wang, et al., Tunable Schottky barrier in graphene/graphene-like germanium carbide van der Waals heterostructure, Sci. Rep. 9 (2019) 1–7.
[61] A. Bafekry, M. Neek-Amal, Tuning the electronic properties of graphene-graphitic carbon nitride heterostructures and heterojunctions by using an electric field, Phys. Rev. B 101 (2020) 1–10.
[62] Q. Guo, G. Wang, R. Pandey, S.P. Karna, Robust band gaps in the graphene/oxide heterostructure: SnO/graphene/SnO, Phys. Chem. Chem. Phys. 20 (2018) 17983–17989.
[63] S. Mukherjee, L. Kavalsky, C.V. Singh, Ultrahigh Storage and Fast Diff usion of Na and K in Blue Phosphorene Anodes, ACS Appl. Mater. Interfaces 10 (2018) 8630–8639.
[64] M. Sun, U. Schwingenschlögl, B_2P_6: A Two-Dimensional Anisotropic Janus Material with Potential in Photocatalytic Water Splitting and Metal-Ion Batteries, Chem. Mater. 32 (2020) 4795–4800.

[65] M. Sun, Y. Yan, U. Schwingenschlögl, Beryllene: A Promising Anode Material for Na- and K-Ion Batteries with Ultrafast Charge/Discharge and High Specific Capacity, J. Phys. Chem. Lett. (2020) 9051–9056.
[66] X. Zhang, et al., Insights into the Storage Mechanism of Layered VS_2 Cathode in Alkali Metal-Ion Batteries, Adv. Energy Mater. 10 (2020) 1–8.
[67] S. Thinius, M.M. Islam, P. Heitjans, T. Bredow, Theoretical Study of Li Migration in Lithium − Graphite Intercalation Compounds with Dispersion-Corrected DFT Methods, J. Phys. Chem. C (2014) 1–8.
[68] A. Kordatos, N. Kelaidis, A. Chroneos, Migration of sodium and lithium interstitials in anatase TiO_2, Solid State Ionics 315 (2018) 40–43.
[69] P. Wu, P. Li, M. Huang, Potential Application of Graphene/Antimonene Herterostructure as an Anode for Li-Ion Batteries : A First-Principles Study, nanomaterials 9 (2019) 1–16.
[70] S. Wang, B. Yang, H. Chen, E. Ruckenstein, Popgraphene: A new 2D planar carbon allotrope composed of 5-8-5 carbon rings for high-performance lithium-ion battery anodes from bottom-up programming, J. Mater. Chem. A 6 (2018) 6815–6821.
[71] I. Demiroglu, C. Sevik, New Platform for Ion Battery Applications, J. Phys. Chem. Lett. 10 (2019) 727–734.
[72] J. Ma, J. Fu, M. Niu, R. Quhe, MoO_2 and graphene heterostructure as promising flexible anodes for lithium-ion batteries, Carbon N. Y. 147 (2019) 357–363.
[73] X. Wu, F. Kang, W. Duan, J. Li, Density functional theory calculations: A powerful tool to simulate and design high-performance energy storage and conversion materials, Prog. Nat. Sci. Mater. Int. 29 (2019) 247–255.
[74] Q. Cheng, Y. Okamoto, N. Tamura, M. Tsuji, S. Maruyama, Y. Matsuo, Graphene-Like-Graphite as Fast-Chargeable and High-Capacity Anode Materials for Lithium Ion Batteries, Sci. Rep. 7 (2017) 1–14.
[75] C. He, J.H. Zhang, W.X. Zhang, T.T. Li, GeSe/BP van der Waals Heterostructures as Promising Anode Materials for Potassium-Ion Batteries, J. Phys. Chem. C 123 (2019) 5157–5163.
[76] Z. Jian, W. Luo, X. Ji, Carbon Electrodes for K-Ion Batteries, J. Am. Chem. Soc. 137 (36) (2015) 11566–11569.
[77] Y. Sun, N. Liu, Y. Cui, Promises and challenges of nanomaterials for lithium-based rechargeable batteries, Nat. Energy 1 (2016) 1–12.
[78] X.H. Liu, et al., In situ atomic-scale imaging of electrochemical lithiation in silicon, Nat. Nanotechnol. 7 (2012) 749–756.
[79] B. Qiu, X. Zhao, G. Hu, W. Yue, J. Ren, X. Yuan, Optical Properties of Graphene/MoS_2 Heterostructure : First Principles Calculations, Nanomaterials 8 (2018) 1–10.
[80] F. Zhang, Tuning the Schottky contacts at the graphene/WS_2 interface by electric field, RSC Adv 7 (2017) 29350–29356.
[81] M. Sun, J. Chou, J. Yu, W. Tang, Effects of structural imperfection on the electronic properties of graphene/WSe_2 heterostructures, J. Mater. Chem. C (2017) 42–46.
[82] Y. Aierken, C. Sevik, O. Gülseren, F.M. Peeters, D. Çakir, MXenes/graphene heterostructures for Li battery applications: A first principles study, J. Mater. Chem. A 6 (2018) 2337–2345.